Available online at www.sciencedirect.com

jmr&t Journal of Materials Research and Technology

journal homepage: www.elsevier.com/locate/jmrt

Original Article

Pore morphology evolution and atom distribution of doped Fe_2O_3 foams developed by freeze-casting after redox cycling

P.J. Lloreda-Jurado, Jesús Hernández-Saz, E. Chicardi, A. Paúl, R. Sepúlveda *

Departamento de Ingeniería y Ciencia de los Materiales y del Transporte, E.T.S. de Ingenieros, Universidad de Sevilla, Avda. Camino de los Descubrimientos s/n., 41092 Sevilla, Spain

ARTICLE INFO

Article history:
Received 5 March 2021
Accepted 3 June 2021
Available online 9 June 2021

Keywords:
Chemical looping system
Fe_2O_3
Pore evolution
Freeze-casting
Camphene
Al_2O_3

ABSTRACT

Chemical looping water splitting systems operate at relatively high temperatures (450 −800 °C) to produce, purify, or store hydrogen by the cyclic reduction and oxidation (redox) of a solid oxygen carrier. Therefore, to improve long-term operation, it is necessary to develop highly stable oxygen carriers with large specific surface areas. In this work, highly interconnected doped Fe_2O_3 foams are fabricated through the freeze-casting technique of a submicrometric camphene-based suspension to prevent Fe sintering and pore clogging during redox operation. The influence of the dopant elements (Al and Ce) over the pore morphology evolution, and redox performances are examined. The use of an Fe_2O_3 porous structure with initial pore size above 100 microns shows a significant reduction of the sample densification, and the addition of Al_2O_3 by the citrate method prevent the rapid formation of an Fe_3O_4 layer at the foams struts that diminish the reoxidation rate step in the redox processing.

1. Introduction

In recent decades, the reduction of CO_2 emissions from fossil-fuel consumption has become a necessity due to the undeniable effects of global warming [1]. Switching to a clean and renewable energy source is an unavoidable route to counterbalance this harmful effect. Hydrogen seems a valid alternative, since no CO_2 is emitted at its consumption, although current large-scale production is still based on reforming methane, oil, or coal [2]. Therefore, a more realistic option for cleaner hydrogen production involves utilising renewable (or CO_2 neutral) resources in combination with carbon-capture systems [3]. The Chemical-Looping Water-Splitting process (CLWS) or Steam-Iron Process (SIP), wherein iron is employed, are promising technologies for hydrogen production and/or purification that can combine both these technological requirements. The SIP is a two-step process, where first a suitable solid oxide (i.e., an oxygen carrier) is exposed to a reducing gas stream to turn it into metal iron. The gas stream

* Corresponding author.
E-mail address: rsepulveda@us.es (R. Sepúlveda).
https://doi.org/10.1016/j.jmrt.2021.06.008

could be a mixture of hydrogen and CO, commonly referred to as syngas [4]. A steam flow then re-oxidizes the Fe into iron oxide and produces pure hydrogen by splitting the water molecule. Finally, the re-oxidized iron oxide is employed to restart the process.

Hematite (Fe_2O_3) presents an attractive oxygen carrier capability for the production, purification, or storage of hydrogen by SIP since it is abundant and inexpensive and also due to its redox properties [5–7]. Iron could act as a secondary source of hydrogen storage if it is oxidized by steam to form Fe_3O_4 and if the hydrogen released is then collected, theoretically, at standard temperature and pressure conditions, whereby 0.534 L of H_2 can be stored per gram, which is comparable with the storage density of conventional metal hydrides [8]. Nonetheless, the performance of Fe_2O_3 as an oxygen carrier is deeply affected by the sintering phenomena, also called deactivation, since many applications require numerous redox cycles at high temperatures.

In order to prevent or delay particle sintering and to control the redox reaction kinetic, many studies have doped the hematite with diverse elements, such as Al [9], Ce [10,11], Zr [12], Mo [13], La [14], and Ca [15,16]. Other researchers have demonstrated the use of structural porous materials as oxygen carriers to replace the fluidized-bed systems. Honeycomb monoliths [10,17] and Fe_2O_3 foams [18] proved to possess comparable redox performances.

CeO_2 as an additive induces crystal modification and stabilisation of the iron oxides [19], despite the limited solubility observed among Fe_xO and CeO_2 phases since Fe^{3+} ions can be incorporated at the CeO_2 fluorite crystal structure at lattice (Ce^{4+}) and interstitial position by hydrothermal [20] or co-precipitation [21] routes rather than by the standard milling process. Furthermore, during high temperature operation, the formation of hematite-like solid solutions and perovskite $CeFeO_3$ phases (Ce^{3+}) is promoted. Therefore, the increase in vacancy concentration enhances the redox performance of Fe_2O_3–CeO_2 systems by higher oxygen mobility [22]. Al_2O_3, as an additive, improves the cycle stability of Fe_2O_3 during continuous operation [7]. Fe_2O_3–Al_2O_3 shows limit solubility: at 1300 °C, about 20 wt% Al_2O_3 can be incorporated into a hematite-like solid solution (H_{ss}) [23], while at room temperature, solubility is neglected. The thermal cycling induced the formation of hercynite ($FeAl_2O_4$) [24], which has a spinel crystal structure where Fe and Al occupy divalent and trivalent cation positions. This spinel phase is more favourably formed during the reduction reaction and early stage of the oxidation reaction since Fe and FeO phases react exothermically in the presence of Al_2O_3. In the case of the Fe_3O_4–Al_2O_3 system, a miscibility gap is formed below 860 °C and two phases are found: magnetite-based solid solution (M_{ss}) and hercynite. At 750 °C, M_{ss} shows a solubility maximum of 12 wt % Al_2O_3. The use of up to 3 wt% Al_2O_3 enhances the reduction process of Fe_3O_4 due to the formation of a network-like structure of wüstite [25,26].

Freeze-casting (FC) is a promising manufacturing technique for the production of porous materials with a wide variety of porosity range, pore size, and morphology [27,28]. It is also cost-effective, eco-friendly, and scalable on an industrial level. However, pure Fe-foams manufactured by FC using water [29] and camphene-based [30,31] hematite slurries have shown significant modification of the pore structure after being subjected to several redox cycles. Authors have found a continuous reduction in the pore size due to the sintering of the Fe cell walls, which is especially critical when initial pore sizes were under 30 μm in diameter. Nevertheless, Lloreda-Jurado et al. [32] have reported doped Fe_2O_3 foams manufactured by FC with diameter pore sizes from 30 to 130 μm, simply by controlling the processing parameters.

Therefore, the aim of this research is to determine the influence of the redox cycling over the pore morphology and atom distribution on doped Fe_2O_3 foams manufactured by FC with initial pore sizes above 100 μm. The Fe_2O_3 powder doped with Al and Ce was synthesized by the citrate method and subsequently suspended in camphene.

2. Experimental procedure

2.1. *Powder synthesis*

Doped Fe_2O_3 powder is fabricated using the citrate method previously described by Lorente et al. [33]. Initially, aqueous solutions of selected metal nitrates and citric acid are stirred at 80 °C until a gel is obtained. The resulting gel is dried at 110 °C overnight and then calcined at 350 °C for 2 h followed by a final step of 700 °C for 6 h to ensure a good level of crystallinity. The resulting powder, *as-synthesized*, is later crushed and sieved to separate particles within 160–200 μm in diameter. The final powder composition is approximately 98 wt% Fe_2O_3, 1.75 wt% Al_2O_3, and 0.25 wt% CeO_2.

2.2. *Sample preparation*

Doped Fe_2O_3 foams were fabricated using the freeze-casting method previously described by Lloreda-Jurado et al. [32]. The method starts by a further reduction of the particle size by ball milling down to 0.2 μm in diameter. A 5 vol.% powder suspension in camphene (Sigma Aldrich, Spain) is then obtained by ball-milling at 60 °C for approximately 12 h. First 3 wt% of dispersant agent KD4 (oligomeric polyester provided by CRODA Ibérica) is mixed for 30 min in camphene, and the powder is subsequently incorporated and ball-milled for 8 h. Finally, 20 vol.% polystyrene (Sigma Aldrich, Spain) with a $M_W = 350{,}000\ g\ mol^{-1}$ was added as a binder and mixed for another 3 h. Both organic additives were formulated according to the initial powder load and were incorporated sequentially to aid in the proper particle dispersion. The camphene suspension was then poured into a 30 mm in diameter by 15 mm in height PFTE mould, preheated at 60 °C placed inside an incubator. Directional solidification was promoted by running water at 42.5 °C through the mould base and gradually reducing the incubator temperature until reaching complete sample solidification. A slow solidification rate was employed to enhance pore enlargement during the FC process. Finally, after demoulding, and a 3-day camphene sublimation process at ambient conditions under forced airflow, the sample is sintered in air at 600 °C for 2 h for organic-specimen burn-out, plus a sintering of 1100 °C for 2 h for particle sintering. After the sintering, the sample *as-fabricated* measures approximately 9 mm in height by 24 mm in diameter.

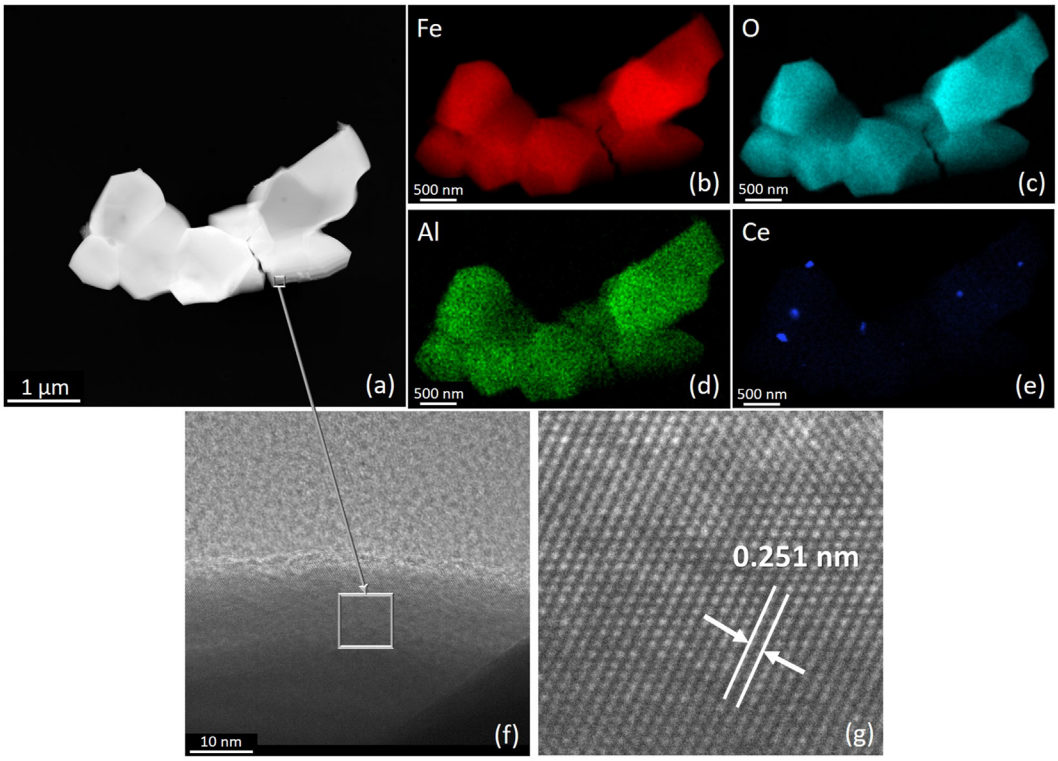

Fig. 1 – HAADF-STEM image of the initial doped Fe_2O_3 powder (*as-synthesised*) showing an aggregate of particles. (a) EDX analysis shows the distribution of the principal elements: Fe (b), O (c), Al (d), and Ce (e). An HRTEM image of a selected area of the particle (f), displays the atomic arrangement of the crystal plane (110) (g).

2.3. *Microstructural and redox performance characterisation*

The pore morphology characterisation of the as-fabricated sample is determined by Optical Microscopy (OM) and Field Emission Scanning Electron Microscopy (FESEM) across the entire height. Initial pore size and cell wall width were determined by OM images using the non-redundant maximum-sphere-fitted algorithm [34] of the ImageJ software. To estimate the average pore diameter at different areas of the sample height, 5 OM images covering an area of approximately 4 mm^2 in total were used.

In turn, the redox behaviour is determined on subsamples of 1.2 mm × 1.2 mm × 4.5 mm, sectioned from the centre-top part of the as-fabricated sample (to reduce the presence of pores under 50 μm in diameter), while maintaining the freezing direction parallel to the longest dimension. Some additional manual grinding was necessary to obtain a 20 mg subsample. This study is carried out in a thermogravimetric analyser (TG) Netzsch® STA 449 F3 Jupiter using an alumina plate as support for the porous subsample. Two redox conditions, dynamic and isothermal, were analysed under the following setup: 1) Dynamic: reduction up to 700 °C with a gas flow of N_2-20 vol.% H_2, followed by an oxidation up to 800 °C with a gas flow of N_2-12 vol.% H_2O. Data points were collected at a rate of 5 data s^{-1}. 2) Isothermal: 3 consecutive cycles of reduction at 750 °C, and oxidation at 450 °C. Data points were collected at a rate of 12 data s^{-1}. Heating rate and flow rates were established at 5 °C/min and 100 NmL/min, respectively. In both redox conditions, the porous samples were removed from the STA after the oxidation stage is completed. Two subsamples were tested at each redox condition.

After the redox test, subsamples were subjected to X-ray computed tomography (X-CT) to determine the pore morphology variation using a YXLON micro-tomograph model Y.COUGAR-SMT. Optical configuration achieved a voxel of 7.56 μm/pixel with the X-ray source operating at 52 KV and 10.09 μA. The subsamples were rotated 360° over the largest axis to obtain 1440 projections during approximately 49 min of scan, the collected 2D cross-sectional images were pre-processed with ImageJ software (8-bit binarisation, threshold, and removal of 1-pixel outliers), and 3D visualisations were made using Avizo software.

Dopant element distribution was determined by Transmission Electron Microscopy (TEM) in the as-synthesised and as-fabricated condition. An FEI TALOS F200S is used operating at 200 kV with a field emission gun and equipped with Super-X dispersive X-ray spectrometry systems including two silicon drift detectors (FEI ChemiSTEM), provided with their specific software for acquisition and data processing (Thermo Scientific Velox®). The Crystallography Open Database was used to identify the unknown planes of the CeO_2 and iron oxide particles.

Subsequently, X-ray Photoelectron Spectroscopy (XPS) is employed to determine the oxidation state and chemical content of doped Fe_2O_3 in the *as-synthesised*, *as-fabricated*, and

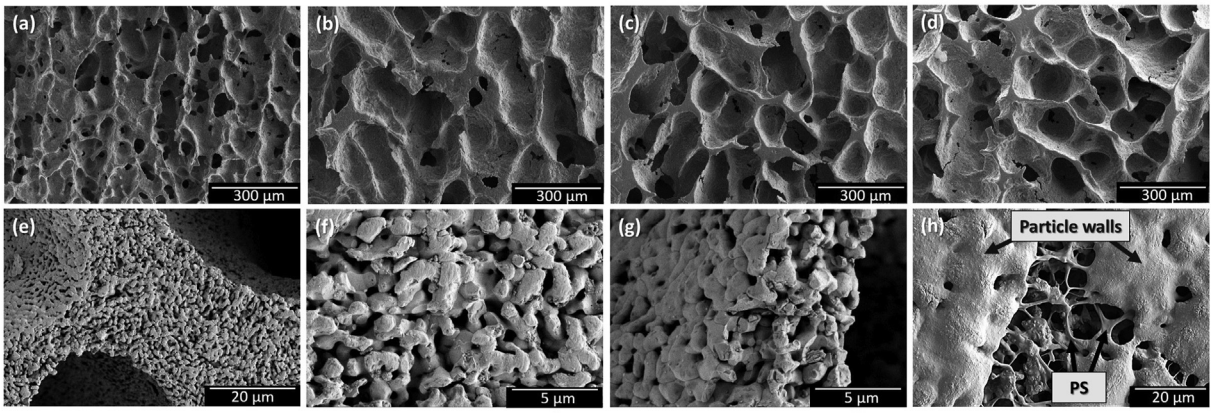

Fig. 2 – SEM micrographs of *as-fabricated* doped Fe_2O_3 foams at different sample heights: 0 mm (a), 3 mm (b), 6 mm (c), and 9 mm (d). Details of the porous cell-wall surface (e, f) and cross-section (g) are shown. Micrographs a-d were taken using the same magnification. Doped Fe_2O_3 foams before sintering (h) shown PS aggregated into the particle walls and forming struts across them.

after isothermal redox processing specimens. A SPECS Hemispherical Energy Analyzer model Phoibos 150 MCD is used. The deconvolution of XPS spectra is performed according to the Gaussian–Lorentzian Cross Product expression as a fitting function (E.q.1) using PeakFit software (Systat Software Inc.)

$$y = \frac{a_0}{1 + a_3\left(\frac{x-a_1}{a_2}\right)^2 exp\left[(1-a_3)\frac{1}{2}\left(\frac{x-a_1}{a_2}\right)^2\right]} \quad (1)$$

where a_0 is the amplitude, a_1 is the centre of the curve, a_2 is the width ($a_2 > 0$), and a_3 is related to the shape of the curve ($0 \leq a_3 \leq 1$, the pure Lorentzian occurs with $a_3 = 1$ and the pure Gaussian occurs with $a_3 = 0$).

Finally, X-Ray Diffraction (XRD) was performed to bear out phase evolution in the *as-fabricated* and *after isothermal redox* processing samples. Previous to the XRD study, the specimens were mechanically milled to ensure the sample representativeness. XRD patterns were recorded using a PANalytical X'Pert Pro instrument (Malvern Panalytical Ltd, Malvern, UK) equipped with a Bragg–Brentano θ/θ geometry, Cu-Kα radiation source (45 kV, 40 mA), secondary Kβ filter and using a X'Celerator detector. The XRD patterns were obtained in 2 theta degree configuration by scanning between 20° and 120° with 0.03° steps and a counting time of 800 s·step^{-1}. The open-access Crystallography Open Database (COD) was employed to elucidate the crystalline phases developed together with their corresponding structure and space-group symmetries (SGSs). A lanthanum hexaboride, LaB_6 (Standard Reference Material 660b, NIST) pattern is utilised to calibrate the positions of the diffraction lines.

3. Results and discussion

3.1. *Doped Fe_2O_3 powder characterisation:* as-synthesised

Figure 1a shows a High-Angle Annular Dark-Field (HAADF) image in Scanning TEM mode obtained from an aggregate of doped Fe_2O_3 particles that exhibit an average size of 0.2 μm in diameter. The element distribution analysis performed by EDX shows a uniform distribution of Fe, O, and Al (Fig. 1b–c), while Ce is segregated to a different location at the particle surface (Fig. 1e). These results suggest that Ce atoms were depleted from the Fe_2O_3 matrix during particle synthesis. This is reasonable since oxide phases can be separated during annealing at temperatures above 600 °C [35,36]. The doped Fe_2O_3 particle (Fig. 1f) shows an interplanar distance of 0.251 nm (Fig. 1g), in agreement with the plane 110 of pure bulk α-Fe_2O_3. Some minor lattice distortion is detected in other interplanar distances. This is due to Al ions (with smaller ionic radii) randomly occupying cation positions in the rhombohedral crystal structure of α-Fe_2O_3. This result corroborates the formation of a $(Fe,Al)_2O_3$ solid solution described in the literature [23,37].

3.2. *Doped Fe_2O_3 foam characterisation:* as-fabricated

During FC, the directional solidification imposed on the slurry created a unique pore structure. The growing camphene dendrites push the particles into the interdendritic spaces and form particle aggregates that replicate the dendrite morphology. Since the sample heat is extracted through the bottom by a constant-temperature flow of water during solidification, the incubator temperature was continuously reduced as well. The thermal gradient decreased and the solidification front velocity increased across the sample height. This situation promotes the formation of an equiaxed and interconnected porous structure, where the average pore size increases significantly with the sample height as the solidification front moves a few millimetres away from the sample base, as shown in Fig. 2a–b. Average pore diameters were calculated in areas described by Fig. 2a–d, as 29, 100, 117, and 127 μm, respectively. ANOVA and Tukey test of the pore size variation along the sample height showed a calculated *p-value*, $q_{0.05}$, and *critical-value* of 0.0022, 4.05, and 66 μm respectively. Therefore, there is significant difference in pore size at the bottom (Fig. 2a), but non along the rest of the sample height

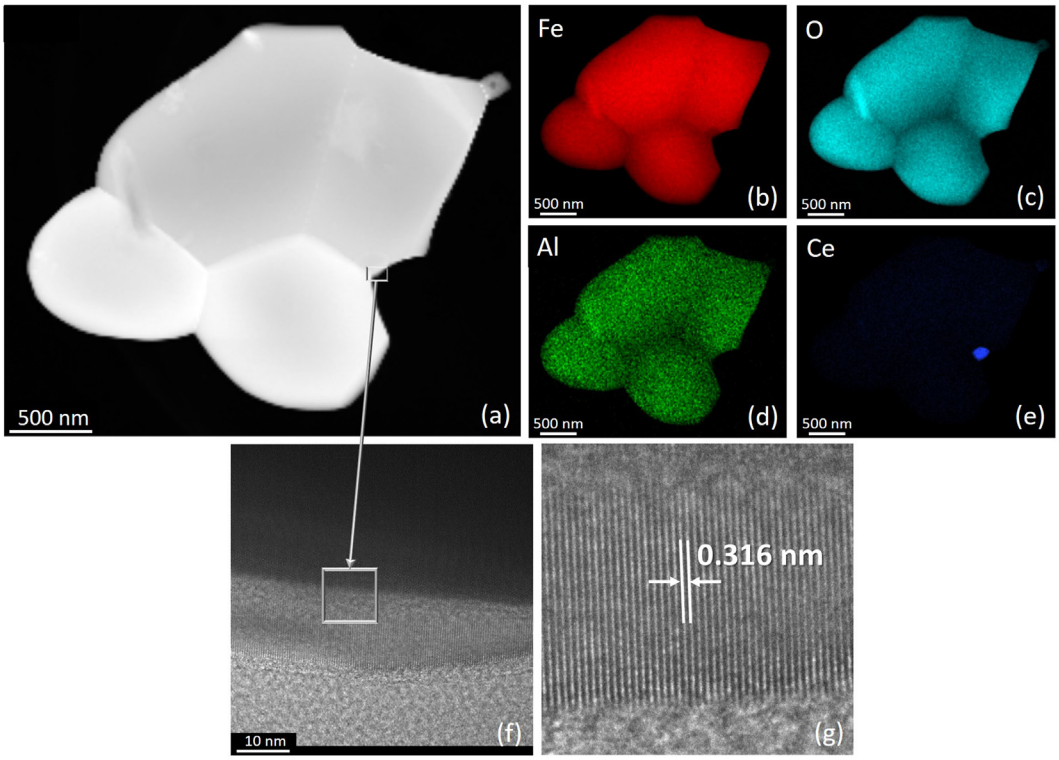

Fig. 3 – HAADF-STEM image of the doped Fe_2O_3 foam (*as-fabricated*) showing an aggregate of particles (a). EDX analysis shows the principal element distribution: Fe (b), O (c), Al (d) and Ce (e). The HRTEM image of the selected area of a CeO_2 particle on (f) displays the atomic arrangement of the crystal plane (111) (g).

(Fig. 2b–d). The average thickness of the cell wall showed a much wider size distribution along the sample, from minimum values of 3–4 μm to a maximum of 60 μm.

Regardless of the position, the cell wall (Fig. 2e) exhibited a highly porous structure on its own. An interconnected pore structure with diameters less than 1 μm is observed at the cell-wall surface (Fig. 2e–f) and its cross-section (Fig. 2g). This secondary porosity is attributable to the pyrolization of C-based compound incorporated through the foam fabrication. A gas adsorption analysis performed in the *as-fabricated* material using a Micromeritics ASAP 2420 (N_2 adsorption at 77 K) have shown a BET surface area of 0.613 m^2/g, much higher than those previously reported for pure hematite scaffolds fabricated under similar conditions [18]. During slurry preparation, dispersant agent and PS were added at different moments of the ball-milling procedure. First, the dispersant agent was added at the beginning of the dispersion process, and after 8 h of ball-milling the polystyrene (PS) is incorporated. KD4 is an oligomeric polyester with a C66 long chain, and displays good adsorption properties due to its carboxylic acid group. This carboxylic group is anchored to the doped Fe_2O_3 particle surfaces leading to a high steric barrier approximately above 10 nm [38]. Since PS has phenyl functional groups every two C atoms and camphene is a bicyclic skeleton monoterpene, both dispersant and binder show good chemical affinity. The melted camphene forms a non-polar solvent where the PS polymer chains were disentangled (dissolved). Doped Fe_2O_3 particles could be trapped by the PS long C–C chain due to the hydrogen bond driven by the KD4 previously anchored. Moreover, during directional solidification of camphene, 20 vol.% PS was incorporated into the particles walls and formed struts across them, as showed in Fig. 2h.

The sintering process volatilises the C-based species and some carbonaceous reductant gases are produced at even relatively low temperatures [39]. KD4 and PS have a chemical formulation of $C_{90}H_{172}O_{10}$ and $(C_8H_8)_{n\text{-}1}$ respectively, and therefore a certain level of carbothermic reduction could be expected according to Bell's Diagram for the Fe–C–O [40], where the magnetite phase remains stable at temperatures lower than 570 °C and $CO/(CO + CO_2)$ gas ratio below 0.5, but no traces of Fe_3O_4 is detected by TEM analysis after sintering (i.e., a nearly 0% degree of reduction). In this work, the mole ratio of C/O described as the carbon contend at the KD4 and PS by the oxygen at the hematite is equal to 0.2, which is lower than the value referred to in other studies (0.63 [39] or 1 [41]) with a degree of reduction above 55%. This result suggests that reductant gases produce during the sintering process, even the close integration between solid particle and C-based species achieved by the slurry preparation, were insufficient to promote a significant reduction reaction, despite the close integration between solid particle and C-based species during slurry preparation and the FC procedure.

Figure 3a shows an HAADF-STEM image of an aggregate of particles where the sintering exerts no significant effects on the doped element distribution. The EDX analysis performed (Fig. 3b–e) on several particles shows a persistent homogeneous distribution of the Al atoms (Fig. 3d), and Ce atoms forming individual clusters (Fig. 3e). The HRTEM image of Fig. 3f shows the crystalline structure of a CeO_2 particle. A detailed magnification of the CeO_2 particles is shown in Fig. 3g. The distant measures correspond to planes (111) of stoichiometric CeO_2.

3.3. *Doped Fe_2O_3 foam characterisation:* after the redox process

During dynamic redox processing (Fig. 4a), doped Fe_2O_3 foam initiates its reduction at 448 °C, which is a higher temperature than that of the powder version (300 °C), and the step reaction of hematite to magnetite to iron is inhibited. However, both were completed around 600 °C. While the temperature kept rising from 600 °C to 700 °C, a sintering process on the formed Fe walls is definitely encouraged. Since most redox processing

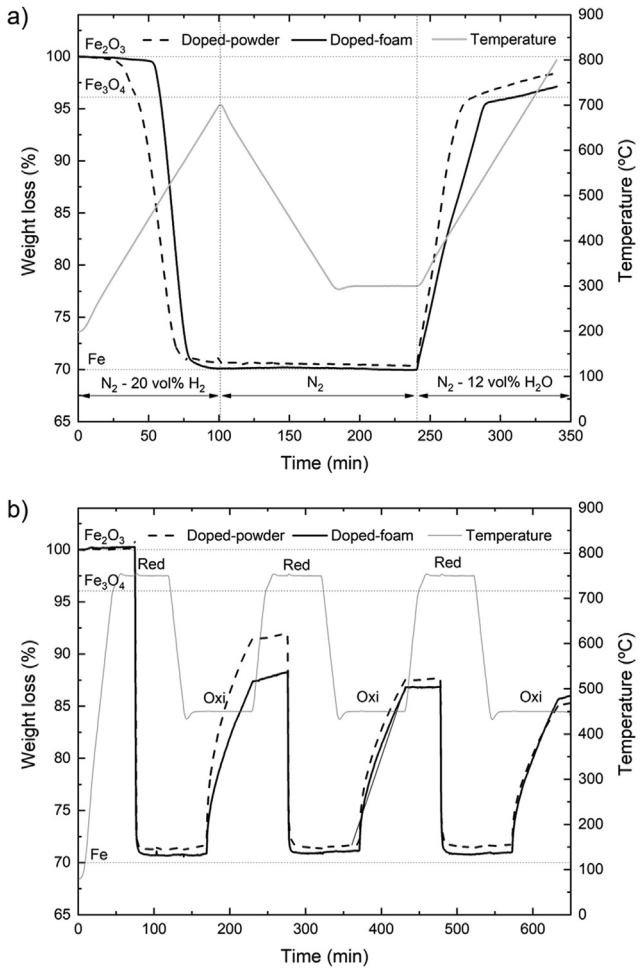

Fig. 4 – Weight changes of Doped Fe_2O_3 foam under dynamic (a) and isothermal (b) redox condition. The doped powder behaviour has been included as a comparison. Fe_2O_3, Fe_3O_4, and Fe theoretical weight lines were incorporated as reaction guidelines.

under SIP conditions are performed at temperatures from 700 °C to 900 °C, there is a clear evidence that regardless of the morphology of the oxygen carrier, a sintering process (i.e., efficiency loss) is inevitably encountered. Through the oxidation reaction, both foam and powder reach a maximum weight gain corresponding to Fe_3O_4: this oxide phase is already predicted by the Bell Diagram [40], and has previously been reported by other authors [40,42] in the case of steam oxidation. The use of a foam morphology shows a decrease on the kinetic reaction, while the subsequent formation of iron oxides layers on top of the Fe cell walls limit the access of steam to fresh Fe. Moreover, at 634 °C, the oxidation reaction to Fe_3O_4 could be considered completed.

The isothermal redox processing (Fig. 4b) shows weight loss and gain with the alternate reduction and oxidation reaction in the doped foam and powder, respectively. As discussed previously, the reduction reaction at 750 °C converts Fe_2O_3 into metallic Fe, while the steam re-oxidation at 450 °C allows the conversion to Fe_3O_4. Thus, a maximum theoretical value of 97% weight change could be achievable during oxide conversion. In the first redox cycle, Fe_2O_3 turns suddenly into Fe in just 5 min within the initial 30 min of reduction. However, the oxidation step takes almost 1 h to recover 88% of the weight lost. With the second and third redox cycle, the reduction reaction is again abrupt and nearly completed to metallic Fe in minutes, and the re-oxidation reactions takes place in 1 h, whereby 86% of the weight lost is recovered. In contrast with the powder version, where reduction and oxidation reaction follows the same trend as the foams, the redox performance dropped significantly with the cycling, from 92% in the first cycle to 85% in the third cycle. The doped Fe_2O_3 has demonstrated a more regular and steadier redox performance, by mitigating the decrease in the oxygen weight gain in the redox cycles. Additionally, the foam is entirely converse to metallic Fe after every reduction reaction, as is the re-oxidation reaction which is primarily limited by the access to fresh Fe, among other thermodynamic considerations. Indeed, the decrease in redox performance is usually attributed to a variety of factors, such as: 1) the reduction temperature, especially above 600 °C, promotes the sintering of the Fe walls thereby reducing the porosity, especially those observed in Fig. 2e–g; 2) The Fe_2O_3 creates a core–shell structure [43] during redox cycling, which segregates Ce and Al oxides species into the grain boundaries, and ultimately to the wall interiors, due to the lack of solubility. As discussed earlier, Ce atoms were segregated from the $(Fe,Al)_2O_3$ solid solution during the powder synthesis and foam consolidation heat treatments. Therefore, the improvement in the oxygen mobility and storage capacity expected from the addition of CeO_2 [44,45] could decrease due to the reduction in the number of interfaces Fe_3O_4/CeO_2. Likewise, aluminium atoms were highly scattered in the doped Fe_2O_3 powder and foam due to the citrate method employed during their synthesis. Al_2O_3 prevents the formation of a dense iron shell by promoting a reduction step in the sample surface, from magnetite to a network-like structure of wüstite, and, finally, to iron [26,46], thereby delaying the sintering of the fresh Fe particles [47]. These aspects could counterbalance the noteworthy metal sintering during the reduction step, and decrease the loss of redox performance.

The pore morphology evolution of the samples subjected to dynamic and isothermal conditions were characterised by X-

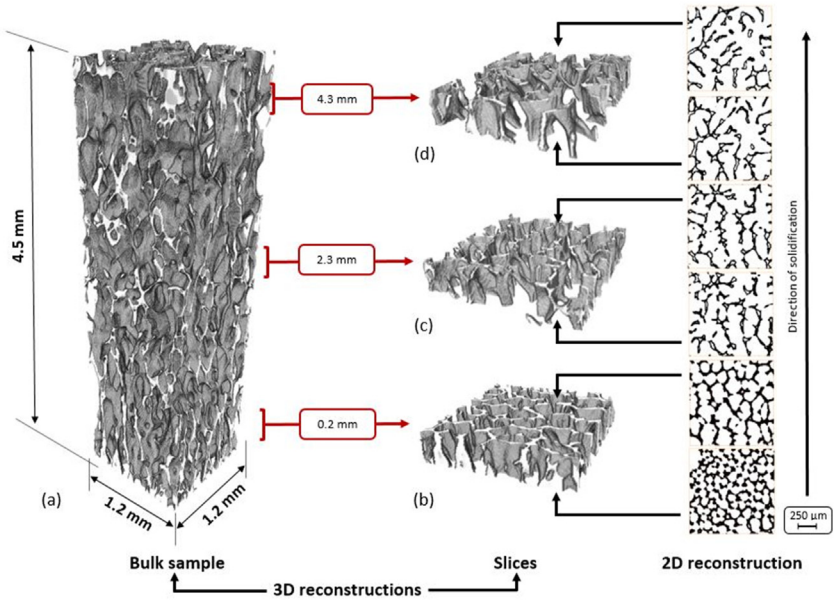

Fig. 5 – 3D reconstructions from X-CT of the doped Fe_2O_3 foams after dynamic redox processing: bulk sample (a) and slices of 250 μm in thickness at different sample heights: (b) 0.2 mm, (c) 2.3 mm and (d) 4.3 mm. The 2D projections are the bottom and top part of the slice reconstructions showing the pore-size evolution.

CT. The subsamples extracted from the doped Fe_2O_3 foams correspond to the top half of the entire sample, where the initial pore size varies from 110 μm at the base to 143 μm at the top. Figure 5a shows the 3D reconstruction of the complete doped Fe_2O_3 foams after the dynamic redox cycles. No significant shrinkage or crack formation is observed. During constant heating, the dynamic redox condition induced a complete reduction of the doped Fe_2O_3 foam to Fe, and a re-oxidation to Fe_3O_4 (magnetite) phase due to thermodynamic limitation. As the slice reconstructions (Fig. 5b–d) show, the pore morphology was kept constant across the sample height. The initial equiaxed and interconnected porous structure observed in Fig. 2 was retained. Moreover, the pore size slightly varies as compared to the initial pore size: the 2D projections show an average pore size of 96, 137, 150, 149, 165, and 157 μm from the bottom to the top specimen, respectively. The average thickness of the cell wall is determined as 48 μm at the sample bottom, and decreases continuously until it reaches 30 μm at the top. This value is overestimated since no cell wall below 20 μm in thickness was detected by this measurement technique, due to the threshold of detection being a voxel size of 7.56 μm. The reduction of the thinner cell walls (>20 μm) might counterbalance the overall shrinkage and expansion effect during this redox cycle. The Fe_2O_3 thinner cell walls could be rapidly integrated into thicker walls at the reduction stage, via the sintering of Fe particles. These results show the minor effect of the dynamic redox processing on the doped Fe_2O_3 foam microstructure, and the beneficial effects of the interconnected pore structure developed by the freeze-casting technique employed in this research, where no significant sample densification or pore clogging were produced.

A distinguishing feature is observed in the sample, more evident in the half-top zone: the formation of a cell wall aperture that creates a new close porosity. These effects have previously been reported [29] on pure Fe samples, but are described here for the first time for doped Fe_2O_3 foams. During reduction, the porosity of the cell walls improves the removal of oxygen, by improving the access to more oxidised material. At peak reduction temperature (700 °C), a complete reduction to metal Fe is feasible and expected, the sintering of Fe particles would be undoubtedly promoted, and the cell walls become denser. In the oxidation stage, the constant formation of Fe_xO phases produces a local volumetric expansion due to the crystal phase conversion and the diffusion of Fe atoms outwards, especially when the re-oxidation leads to the formation of an Fe_2O_3 phase. To accommodate these new phases, they are separated and, eventually, exfoliated from the remaining Fe base. This morphology feature is more evident in the top part of the dynamic redox samples (Fig. 5c–d). As pore size increases, Fe walls can act as flat surfaces since their curvature ratio also increases. Therefore, the local expansion of the new phases could be released normal to the surface and then be exfoliated from the Fe base. When pore size or curvature ratio decreases, the Fe walls might resemble a cylinder, and the same volume expansion could no longer be released normal to the surface, and the Fe_xO grains tend to sinter into a more compact layer, thereby diminishing any opportunity for exfoliation.

After 3 complete redox cycles under isothermal conditions, the doped Fe_2O_3 bulk sample retains the overall interconnected pore structure, as shown in Fig. 6a. The 2D projections (Fig. 6b–d) show average pore sizes of: 56 ± 16, 76 ± 21, 132 ± 34, 138 ± 36, 117 ± 29, and 120 ± 37 μm from the bottom to the top of the sample, respectively. The average thickness of the cell wall shows a higher value at the bottom (55 μm) and top (50 μm) parts, as compared with the centre (40 μm); as discussed previously, this value is overestimated due to the

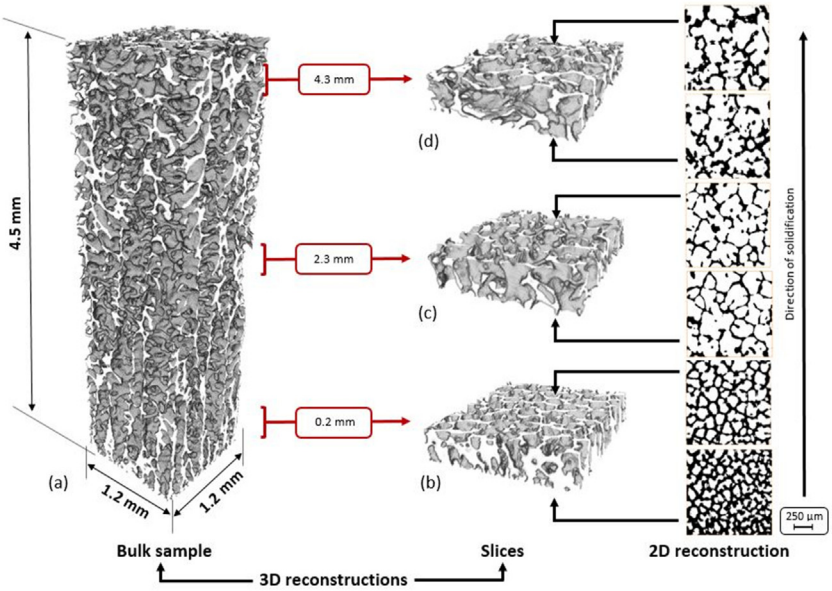

Fig. 6 – 3D reconstructions from X-CT of the doped Fe_2O_3 foams after isothermal redox processing: bulk sample (a) and slices of 250 μm in thickness at different sample heights: (b) 0.2 mm, (c) 2.3 mm, and (d) 4.3 mm. The 2D projections are the bottom and top part of the slice reconstructions showing the pore-size evolution.

measurement technique. In this case, a significant reduction in pore size was observed at the bottom part of the sample, where the initial average pore size passes from nearly 100 μm to 56 μm. As the redox cycles occurred, during the reduction step, the Fe walls thickened, and the pore size and overall porosity decreased due to the rapid sintering at 750 °C. This situation is enhanced at the bottom of the sample, as can be seen in Fig. 6b.

In contrast, the doped foam sample under the dynamic redox condition shows no cell wall aperture across the sample height, which suggests a decrease in the Fe outward mobility to form Fe_xO due to the lower re-oxidation temperature (450 °C), which reduces the possibility of vacancy formation in the cell-wall interiors. In isothermal conditions, the reduction step leads to the formation of Fe_3O_4 preferentially, which decreases the volume expansion during the oxidation reaction and a possible exfoliation. Furthermore, the addition of Al_2O_3 in pure Fe has shown a reduction in the pore formation due to the Kirkendall effect with the conversion of Fe to magnetite [46]. The vacancy diffusion in magnetite is four times lower than in hematite [48], and therefore the Fe outward mobility is considerably reduced.

In each re-oxidation step, some metallic Fe remains unconverted, as shown in Fig. 4b. Therefore, as steam was used for re-oxidation at 450 °C, Fe could be mainly convert to Fe_3O_4 [40] and the remaining metal could be estimated in 9.3 wt% after the first cycle and 11.3 wt% for the remaining second and third cycles, which yield a 6.35 vol.% and 7.80 vol.%, respectively. Figure 7a shows a SEM micrograph of the doped Fe_2O_3 foam surface after the isothermal redox condition. The faceted surface of the magnetite grains is interrupted by a spider-like Fe network; these Fe phases correspond to the unconverted metal. An XRD analysis (Fig. 7b) under both the *as-fabricated* and *after redox process* conditions is carried out to corroborate this assertion. This analysis detects only the hematite phase (Fe_2O_3, R-3c, ref. no. 1546383 in the COD) in the as-sintered specimen. In turn, for the *after redox process* two major phases were elucidated, magnetite (Fe_3O_4, Fd-3m, ref. no. 7228110 in COD) and ferrite (α-Fe, Im-3m, ref. no. 9016601 in the COD). Moreover, slight peaks of unreacted hematite were also detected in this specimen. All these observations therefore corroborate that the initial Fe_2O_3 evolves into Fe_3O_4 with some elemental Fe after the redox cycles. Furthermore, the position of the Fe_2O_3 and Fe_3O_4 peaks were not appreciably displaced, showing no influence of Al or Ce atoms. However, the spider-like Fe network created around the growing magnetite grains does indeed corroborate the influence of the Al atom clusters well-dispersed within the as-sintered sample.

3.4. *XPS characterisation*

The XPS spectra shows the valence state and compositional studies of Fe, Al, and Ce elements in the different stages of the doped Fe_2O_3 *as-synthesised* (before slurry preparation), *as-fabricated* (before FC and sintering), and *after redox processing* (dynamic). Figure 8 shows the high-resolution photoelectron spectrum for Fe2p (a-c) and Al2p (d). The deconvoluted XPS spectra of the as-synthesised (Fig. 8a) and as-fabricated (Fig. 8b) doped Fe_2O_3 powder shows similar convoluted XPS spectra, where peaks at 709.4, 723.1, and 717.3 eV were identified with the Fe^{3+} ions in α-Fe_2O_3 assigned to Fe $2p_{3/2}$, Fe $2p_{1/2}$, and its satellite peak, respectively. The two major peaks for Fe $2p_{3/2}$ and Fe $2p_{1/2}$ are separated by spin energy of 13.7 eV, and the associated satellite peak (717.3 eV) is located at +7.9 eV of the Fe $2p_{3/2}$ peak (709.4 eV), which are in good agreement with the reported value for α-Fe_2O_3 in the literature

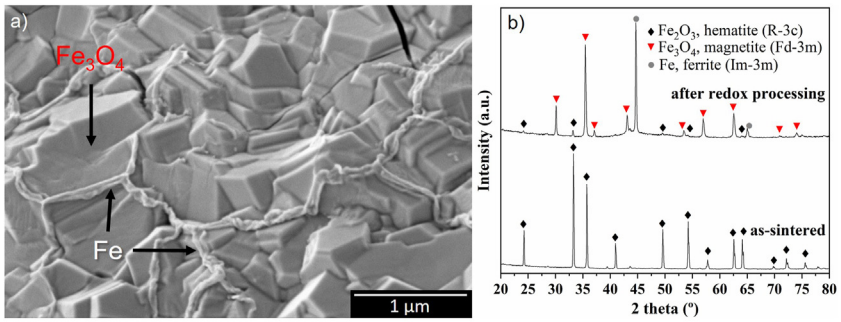

Fig. 7 – SEM micrograph (a) of the doped Fe_2O_3 foams after isothermal redox processing, and XRD patterns (b) for the *as-sintered* and *after redox processing* specimens.

[49,50]. The shake-up satellite (712.8 eV) is also confirmed in the literature for doped Fe_2O_3 prepared by the co-precipitation method from metal nitrate precursors [51] and with the influence of Al^{3+} [52]. In this work, the broadening of the peaks associated with Fe^{3+} to lower binding energies could confirm the change in the oxidation state to Fe^{2+} due to the influence of the Al^{3+} ions being incorporated into the hematite-like $(Fe,Al)_2O_3$ solid matrix. With the sintering process, the satellite peaks of Fe^{3+} in the as-fabricated powder moves to a lower binding energy of 712.5 eV (Fig. 8b) due to the local formation of a near-hercynite ($FeAl_2O_4$) phase on the surface of the particles [24].

After the dynamic redox process (Fig. 8c), the deconvoluted XPS spectrum shows three peaks at 709.5, 716.6, and 723.1 eV corresponding to a non-stoichiometric FeO phase and a peak at 712.1 eV that could be attributed to the aforementioned shake-up satellite. The difference in binding energy between $Fe2p_{3/2}$ (709.5 eV) and the satellite peak (716.6 eV) is 7.1 eV, which is 1.1 eV higher than those values reported for oxidation state Fe^{2+} [50,53]. Nevertheless, the broadening of the $Fe2p_{3/2}$ peak might hinder Fe^{3+} ions corresponding to the Fe_3O_4, since the binding energies are similar. In this regard, the XPS spectrum of the *after redox processing* samples shows a significant broadening of the major peak down to lower binding

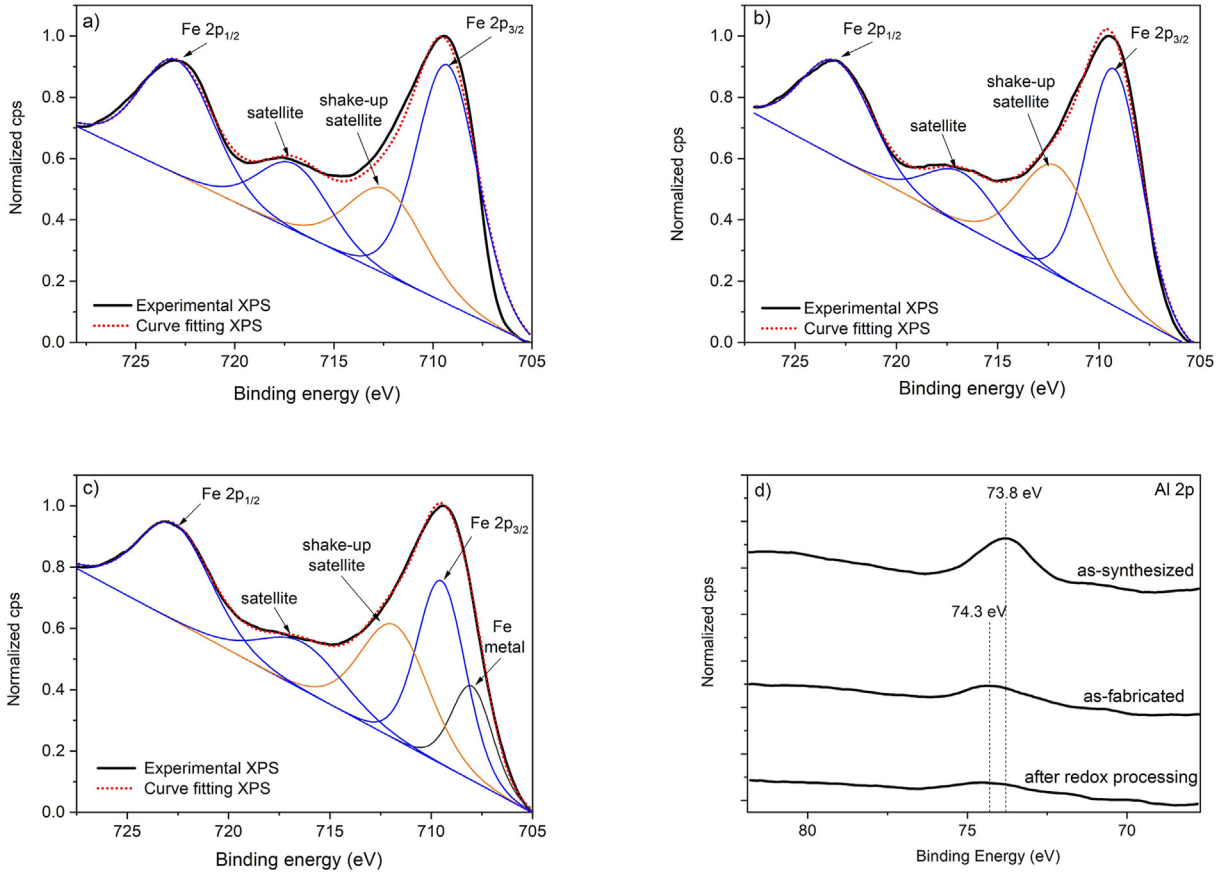

Fig. 8 – High resolution XPS spectra of Fe2p (a–c) for the doped Fe_2O_3 samples as-synthesised (a), as-fabricated (b), and *after redox processing* (c) with the deconvoluted peaks, and Al2p (d) for all samples.

energies, thereby yielding an extra deconvoluted peak at 708.1 eV. This result could be attributed to the presence of metallic iron at the sample surface after the redox cycling [54], which is correlated with the TGA analysis in Fig. 4b, and could confirm the spider-like network of Fig. 7 as metal Fe. The XPS spectrum of Al2p (Fig. 8d) shows a binding energy of 73.8 eV for the *as-synthesised* samples, although for the *as-fabricated* and *after redox processing* samples, the binding energy moves to 74.5 eV. In the as-synthesised powder sample, the Al ions could be in a metallic state due to the low temperature of the final heat treatment (800 °C), which seems sufficient to obtain the Fe_2O_3 crystal. However, after having sintered the powder at 1100 °C and performing the redox processing, the movement of the binding energy to 74.5 eV confirms the formation of $FeAl_2O_4$ on the sample surface [55].

4. Conclusions

Doped Fe_2O_3 foams with potential redox applications were successfully fabricated by FC, and the influences of the Al and Ce atoms in the redox performance was adequately determined.

Al is incorporated into a hematite-like $(Fe,Al)_2O_3$ solid solution in the initial powder, and turns into an $FeAl_2O_4$ phase after the sintering and redox processing. The Al interaction with iron oxide phases reduces the upward mobility of Fe atoms in the cell wall in the doped Fe_2O_3 foam during the re-oxidation step.

No significant influence of CeO_2 on the redox performance was established, since Ce atoms were rapidly depleted to the Fe_2O_3 particle surface, which limits its interaction during redox cycling.

The pore shrinkage is counterbalance by the development of a highly interconnected pore structure above 100 microns using camphene as the media. By increasing the pore size and narrowing the pore-size distribution, the re-oxidation of Fe to Fe_3O_4 is able to accommodate the volume expansion and the exfoliation effects was significantly reduced.

The incorporation of Al atoms into Fe_2O_3 by the citrate method seems to more efficiently preserve the pore morphology in the foam after the redox processing.

Declaration of Competing Interest

The authors declare that they have no known competing financial interests or personal relationships that could have appeared to influence the work reported in this paper.

Acknowledgements

Financial support for this work has been provided by the Ministerio de Ciencia e Innovación – Agencia Estatal de Investigación through the project MAT2016-76713-P co-funded by European Regional Development Fund. Lloreda-Jurado P.J. also thanks to the Universidad de Sevilla for the financial support (grant PIF II.2A, through VI Plan Propio de Investigación). Furthermore, the authors would especially like to thank Dr. Cristina García-Garrido for her contribution in the XPS analysis and dissertation, and Dr. J. A. Peña & J. Herguido for providing the doped Fe_2O_3 powder and their assistance in the redox assay.

REFERENCES

[1] Cook J, Nuccitelli D, Green SA, Richardson M, Winkler B, Painting R, et al. Quantifying the consensus on anthropogenic global warming in the scientific literature. Environ Res Lett 2013;8:024024. https://doi.org/10.1088/1748-9326/8/2/024024.

[2] Kayfeci M, Keçebaş A, Bayat M. Chapter 3 - hydrogen production. In: Calise F, D'Accadia MD, Santarelli M, Lanzini A, Ferrero DBT-SHP, editors. Academic Press; 2019. p. 45–83. https://doi.org/10.1016/B978-0-12-814853-2.00003-5.

[3] Adanez J, Abad A, Garcia-Labiano F, Gayan P, de Diego LF. Progress in chemical-looping combustion and reforming technologies. Prog Energy Combust Sci 2012;38:215–82. https://doi.org/10.1016/j.pecs.2011.09.001.

[4] Li K, Wang H, Wei Y, Yan D. Syngas production from methane and air via a redox process using Ce–Fe mixed oxides as oxygen carriers. Appl Catal B Environ 2010;97:361–72. https://doi.org/10.1016/j.apcatb.2010.04.018.

[5] Otsuka K, Mito A, Takenaka S, Yamanaka I. Production of hydrogen from methane without CO2-emission mediated by indium oxide and iron oxide. Int J Hydrogen Energy 2001;26:191–4. https://doi.org/10.1016/S0360-3199(00)00070-7.

[6] Takenaka S, Kaburagi T, Yamada C, Nomura K, Otsuka K. Storage and supply of hydrogen by means of the redox of the iron oxides modified with Mo and Rh species. J Catal 2004;228:66–74. https://doi.org/10.1016/j.jcat.2004.08.027.

[7] Voitic G, Hacker V. Recent advancements in chemical looping water splitting for the production of hydrogen. RSC Adv 2016;6:98267–96. https://doi.org/10.1039/C6RA21180A.

[8] Barthelemy H, Weber M, Barbier F. Hydrogen storage: recent improvements and industrial perspectives. Int J Hydrogen Energy 2017;42:7254–62. https://doi.org/10.1016/j.ijhydene.2016.03.178.

[9] Liu W, Ismail M, Dunstan MT, Hu W, Zhang Z, Fennell PS, et al. Inhibiting the interaction between FeO and Al2O3 during chemical looping production of hydrogen. RSC Adv 2015;5:1759–71. https://doi.org/10.1039/C4RA11891J.

[10] Long Y, Li K, Gu Z, Zhu X, Wei Y, Lu C, et al. Ce-Fe-Zr-O/MgO coated monolithic oxygen carriers for chemical looping reforming of methane to co-produce syngas and H2. Chem Eng J 2020;388:124190. https://doi.org/10.1016/j.cej.2020.124190.

[11] Zhu X, Wei Y, Wang H, Li K. Ce–Fe oxygen carriers for chemical-looping steam methane reforming. Int J Hydrogen Energy 2013;38:4492–501. https://doi.org/10.1016/j.ijhydene.2013.01.115.

[12] Cho WC, Kim CG, Jeong SU, Park CS, Kang KS, Lee DY, et al. Activation and reactivity of iron oxides as oxygen carriers for hydrogen production by chemical looping. Ind Eng Chem Res 2015;54:3091–100. https://doi.org/10.1021/ie504468a.

[13] Wang H, Zhang J, Wen F, Bai J. Effect of Mo dopants on improving hydrogen production by redox of iron oxide: catalytic role of Mo cation and kinetic study. RSC Adv 2013;3:10341. https://doi.org/10.1039/c3ra22135k.

[14] Gholizadeh A. The effects of A/B-site substitution on structural, redox and catalytic properties of lanthanum ferrite nanoparticles. J Mater Res Technol 2019;8:457–66. https://doi.org/10.1016/j.jmrt.2017.12.006.

[15] Ismail M, Liu W, Dunstan MT, Scott SA. Development and performance of iron based oxygen carriers containing calcium ferrites for chemical looping combustion and production of hydrogen. Int J Hydrogen Energy 2016;41:4073–84. https://doi.org/10.1016/j.ijhydene.2015.11.066.
[16] Sun Z, Chen S, Russell CK, Hu J, Rony AH, Tan G, et al. Improvement of H2-rich gas production with tar abatement from pine wood conversion over bi-functional Ca2Fe2O5 catalyst: investigation of inner-looping redox reaction and promoting mechanisms. Appl Energy 2018;212:931–43. https://doi.org/10.1016/j.apenergy.2017.12.087.
[17] Zhang H, Hong H, Jiang Q, Deng Y, Jin H, Kang Q. Development of a chemical-looping combustion reactor having porous honeycomb chamber and experimental validation by using NiO/NiAl2O4. Appl Energy 2018;211:259–68. https://doi.org/10.1016/j.apenergy.2017.11.053.
[18] Durán P, Lachén J, Plou J, Sepúlveda R, Herguido J, Peña JA. Behaviour of freeze-casting iron oxide for purifying hydrogen streams by steam-iron process. Int J Hydrogen Energy 2016;41:19518–24. https://doi.org/10.1016/j.ijhydene.2016.06.062.
[19] Galvita VV, Poelman H, Bliznuk V, Detavernier C, Marin GB. CeO 2 -modified Fe 2 O 3 for CO 2 utilization via chemical looping. Ind Eng Chem Res 2013;52:8416–26. https://doi.org/10.1021/ie4003574.
[20] Li G, Smith RL, Inomata H. Synthesis of nanoscale Ce1-xFexO2 solid solutions via a low-temperature approach. J Am Chem Soc 2001;123:11091–2. https://doi.org/10.1021/ja016502+.
[21] Pérez-Alonso FJ, López Granados M, Ojeda M, Terreros P, Rojas S, Herranz T, et al. Chemical structures of coprecipitated Fe–Ce mixed oxides. Chem Mater 2005;17:2329–39. https://doi.org/10.1021/cm0477669.
[22] Ma S, Li M, Wang G, Zhang L, Chen S, Sun Z, et al. Effects of Zr doping on Fe2O3/CeO2 oxygen carrier in chemical looping hydrogen generation. Chem Eng J 2018;346:712–25. https://doi.org/10.1016/j.cej.2018.03.171.
[23] Turnock AC, Eugster HP. Fe–Al oxides: phase relationships below 1,000 C. J Petrol 1962;3:533–65. https://doi.org/10.1093/petrology/3.3.533.
[24] Kidambi PR, Cleeton JPE, Scott SA, Dennis JS, Bohn CD. Interaction of iron oxide with alumina in a composite oxygen carrier during the production of hydrogen by chemical looping. Energy Fuels 2012;26:603–17. https://doi.org/10.1021/ef200859d.
[25] Kapelyushin Y, Sasaki Y, Zhang J, Jeong S, Ostrovski O. In-situ study of gaseous reduction of magnetite doped with alumina using high-temperature XRD analysis. Metall Mater Trans B 2015;46:2564–72. https://doi.org/10.1007/s11663-015-0437-4.
[26] Kapelyushin Y, Sasaki Y, Zhang J, Jeong S, Ostrovski O. formation of a network structure in the gaseous reduction of magnetite doped with alumina. Metall Mater Trans B 2017;48:889–99. https://doi.org/10.1007/s11663-016-0897-1.
[27] Li WL, Lu K, Walz JY. Freeze casting of porous materials: review of critical factors in microstructure evolution. Int Mater Rev 2012;57:37–60. https://doi.org/10.1179/1743280411Y.0000000011.
[28] Nelson I, Naleway SE. Intrinsic and extrinsic control of freeze casting. J Mater Res Technol 2019;8:2372–85. https://doi.org/10.1016/j.jmrt.2018.11.011.
[29] Wilke SK, Dunand DC. Structural evolution of directionally freeze-cast iron foams during oxidation/reduction cycles. Acta Mater 2019;162:90–102. https://doi.org/10.1016/j.actamat.2018.09.054.
[30] Um T, Wilke SK, Choe H, Dunand DC. Effects of pore morphology on the cyclical oxidation/reduction of iron foams created via camphene-based freeze casting. J Alloys Compd 2020:156278. https://doi.org/10.1016/j.jallcom.2020.156278.
[31] Lloreda-Jurado PJ, Wilke SK, Scotti K, Paúl-Escolano A, Dunand DC, Sepúlveda R. Structure–processing relationships of freeze-cast iron foams fabricated with various solidification rates and post-casting heat treatment. J Mater Res 2020:1–10. https://doi.org/10.1557/jmr.2020.175.
[32] Lloreda-Jurado PJ, Pérez-Soriano EM, Paúl A, Herguido J, Peña JA, Sepúlveda R. Doped iron oxide scaffolds with gradient porosity fabricated by freeze casting: pore morphology prediction and processing parameters. Mater Sci Technol 2020;36:1227–37. https://doi.org/10.1080/02670836.2020.1765096.
[33] Lorente E, Peña JA, Herguido J. Separation and storage of hydrogen by steam-iron process: effect of added metals upon hydrogen release and solid stability. J Power Sources 2009;192:224–9. https://doi.org/10.1016/j.jpowsour.2008.12.116.
[34] Hildebrand T, Rüegsegger P. A new method for the model-independent assessment of thickness in three-dimensional images. J Microsc 1997;185:67–75. https://doi.org/10.1046/j.1365-2818.1997.1340694.x.
[35] Gobara HM, Aboutaleb WA, Hashem KM, Hassan SA, Henein SA. A novel route for synthesis of α-Fe2O3–CeO2 nanocomposites for ethanol conversion. J Mater Sci 2017;52:550–68. https://doi.org/10.1007/s10853-016-0353-2.
[36] Gu Z, Li K, Qing S, Zhu X, Wei Y, Li Y, et al. Enhanced reducibility and redox stability of Fe 2 O 3 in the presence of CeO 2 nanoparticles. RSC Adv 2014;4:47191–9. https://doi.org/10.1039/C4RA06715K.
[37] Ladavos AK, Bakas TV. The Al2O3-Fe2O3 mixed oxidic system, I. Preparation and characterization. React Kinet Catal Lett 2001;73:223–8. https://doi.org/10.1023/A:1014134601603.
[38] Zürcher S, Graule T. Influence of dispersant structure on the rheological properties of highly-concentrated zirconia dispersions. J Eur Ceram Soc 2005;25:863–73. https://doi.org/10.1016/j.jeurceramsoc.2004.05.002.
[39] Murakami T, Kasai E. Reduction mechanism of iron oxide–carbon composite with polyethylene at lower temperature. ISIJ Int 2011;51:9–13. https://doi.org/10.2355/isijinternational.51.9.
[40] Pineau A, Kanari N, Gaballah I. Kinetics of reduction of iron oxides by H2. Part I: low temperature reduction of hematite. Thermochim Acta 2006;447:89–100. https://doi.org/10.1016/j.tca.2005.10.004.
[41] Wang G, Wang J, Xue Q. Efficient utilization of waste plastics as raw material for metallic iron and syngas production by combining heat treatment pulverization and direct reduction. Process Saf Environ Protect 2020;137:49–57. https://doi.org/10.1016/j.psep.2020.02.017.
[42] Kock AJ, Fortuin HM, Geus JW. The reduction behavior of supported iron catalysts in hydrogen or carbon monoxide atmospheres. J Catal 1985;96:261–75. https://doi.org/10.1016/0021-9517(85)90379-3.
[43] Sun Z, Zhou Q, Fan L-S. formation of core–shell structured composite microparticles via cyclic gas–solid reactions. Langmuir 2013;29:12520–9. https://doi.org/10.1021/la4029832.

[44] Gu Z, Li K, Qing S, Zhu X, Wei Y, Li Y, et al. Enhanced reducibility and redox stability of Fe2O3 in the presence of CeO2 nanoparticles. RSC Adv 2014;4:47191–9. https://doi.org/10.1039/C4RA06715K.

[45] Li K, Haneda M, Gu Z, Wang H, Ozawa M. Modification of CeO2 on the redox property of Fe 2O3. Mater Lett 2013;93:129–32. https://doi.org/10.1016/j.matlet.2012.09.039.

[46] Paananen T, Heinänen K, Härkki J. Degradation of iron oxide caused by alumina during reduction from magnetite. ISIJ Int 2003;43:597–605. https://doi.org/10.2355/isijinternational.43.597.

[47] Theofanidis S, Galvita V, Konstantopoulos C, Poelman H, Marin G. Fe-based nano-materials in catalysis. Materials (Basel) 2018;11:831. https://doi.org/10.3390/ma11050831.

[48] Hallström S, Höglund L, Ågren J. Modeling of iron diffusion in the iron oxides magnetite and hematite with variable stoichiometry. Acta Mater 2011;59:53–60. https://doi.org/10.1016/j.actamat.2010.08.032.

[49] Lu X-F, Chen X-Y, Zhou W, Tong Y-X, Li G-R. α-Fe2O3 @PANI core–shell nanowire arrays as negative electrodes for asymmetric supercapacitors. ACS Appl Mater Interfaces 2015;7:14843–50. https://doi.org/10.1021/acsami.5b03126.

[50] Yamashita T, Hayes P. Analysis of XPS spectra of Fe2+ and Fe3+ ions in oxide materials. Appl Surf Sci 2008;254:2441–9. https://doi.org/10.1016/j.apsusc.2007.09.063.

[51] Moura KO, Lima RJS, Coelho AA, Souza-Junior EA, Duque JGS, Meneses CT. Tuning the surface anisotropy in Fe-doped NiO nanoparticles. Nanoscale 2014;6:352–7. https://doi.org/10.1039/C3NR04926D.

[52] Guo Y, Ali R, Zhang X, Tian W, Zhang L, Lu H, et al. Raman and XPS depth profiling technique to investigate the corrosion behavior of FeSiAl alloy in salt spray environment. J Alloys Compd 2020;834:155075. https://doi.org/10.1016/j.jallcom.2020.155075.

[53] Grosvenor AP, Kobe BA, Biesinger MC, McIntyre NS. Investigation of multiplet splitting of Fe 2p XPS spectra and bonding in iron compounds. Surf Interface Anal 2004;36:1564–74. https://doi.org/10.1002/sia.1984.

[54] Hawn DD, DeKoven BM. Deconvolution as a correction for photoelectron inelastic energy losses in the core level XPS spectra of iron oxides. Surf Interface Anal 1987;10:63–74. https://doi.org/10.1002/sia.740100203.

[55] Velon A, Olefjord I. Oxidation behavior of Ni3Al and Fe3Al: I. XPS calibrations of pure compounds and quantification of the results. Oxid Met 2001;56:415–24. https://doi.org/10.1023/A:1012589315800.